Interlaminar shear fracture of chopped strand mat glass fibre-reinforced polyester laminates

S.Y. ZHANG*, P.D. SODEN† and P.M. SODEN†

(*Chinese Academy of Sciences, People's Republic of China/† UMIST, UK)

The interlaminar shear fracture of chopped strand mat glass fibre-reinforced polyester laminates has been studied both experimentally and analytically. Lap shear (double-grooved) specimens were used to measure the interlaminar shear strength and the cracking mechanism was studied using photomicrography. The finite element method was used to calculate the stress distribution along the shear surface and the mixed-mode stress intensity factors K_I and K_{II}. The length of the shear surface was found to have a significant effect on the results. Based on the experimental and analytical results, the validity of the British Standard for GRP pressure vessels (BS4994, 1973) was evaluated and the critical stress intensity factors K_{Ic} and K_{IIc} for this material were estimated.

Key words: composite materials; shear testing; interlaminar failure; stress analysis; finite element analysis; glass fibres; polyester resins

Chopped strand mat (CSM) glass fibre-reinforced polyester (GRP) is widely used in pressure vessel and pipe line systems for the chemical industry. In burst tests of pressure vessels, bending tests on pipe bends and failure of attachments to GRP vessels, interlaminar failure is often observed. Besides through-thickness tensile failure, interlaminar shear failure deserves consideration as a possible cause of delamination. In the British Standard design code for GRP pressure vessels (BS4994, 1973),[1] a test method for measuring lap shear strength of laminates is specified, but the validity of this method needs to be proved. Chiao and co-workers[2] have used this method to measure the interlaminar shear strength of Kevlar fibre laminates. The data published exhibit wide scatter. Markham and Dawson[3] proposed a simple analytical model for calculating the shear stress distribution along the shear surface. Zhang[4] has studied this problem both experimentally and analytically. The main objective of the present paper is to examine the validity of this method, particularly for CSM glass fibre-reinforced polyester laminates.

The paper consists of two parts, experimental work and a finite element analysis. In the experimental investigation, 28 single lap shear specimens of two different lengths were tested to failure under tension–shear or compression–shear loading and the crack propagation mechanism was studied using photography and photomicrography. In the finite element analysis, the stress distribution along the shear surface was calculated for different lengths of shear surface using orthotropic and isotropic material models, and crack initiation and propagation was studied.

EXPERIMENTAL DETAILS

Specimens

The test materials were flat GRP laminates produced by a commercial fabricator, Plastics Design and Engineering Limited, using Crystic 491 PA polyester resin (from Scott Bader Limited) reinforced with nine layers of 450 g m^{-2} powder-bound glass fibre CSM[5] (Fabmat PB from Fiberglass Limited). The glass fibre content was approximately 30% by weight. Twenty eight specimens in five batches were cut from three different panels (see Table 1). The shape of the specimens is illustrated in Fig. 1. The grooves were cut using a milling machine and had a width of 1.5 mm and a depth of half of the laminate thickness or a little deeper, as specified by BS4994.

Procedure

The tests were carried out in an Instron testing machine under strain-rate control. The cross-head speed was 1–2.54 mm min^{-1}. Standard Instron wedge grips were used for applying tensile loading. For compression–shear tests, the ends of the specimen were gripped in end clamps similar to those specified in BS4994 for compression testing. The clamps prevented

Table 1. Specimen details

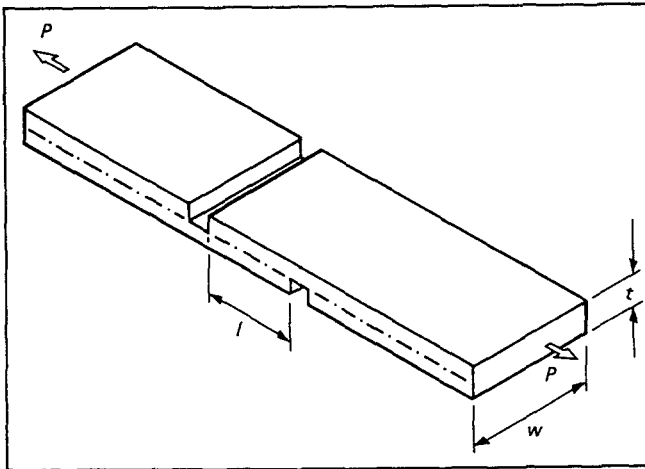| Test method	Panel number	Number of specimens	Length of shear surface, l (mm)	Results, table number
Tension	1	5	12.1	2
Tension	2	6	13.6	3
Tension	1	7	24.4	4
Tension	3	5	12.6	5
Compression	3	5	12.1	6

Fig. 1 Form of the notched shear specimens

Fig. 2 Load vs extension for a tension/shear specimen (specimen no 5.2, cross-head speed 1 mm min^{-1})
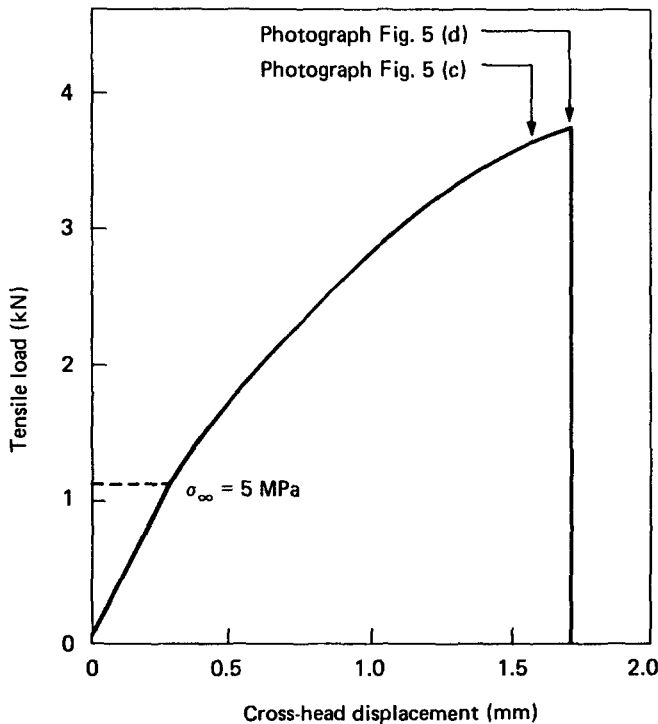
Fig. 3 Load vs displacement for a compression/shear specimen (specimen no 6.1, cross-head speed 1 mm min^{-1})

the ends of the specimen rotating. Load vs elongation (cross-head displacement) curves were recorded automatically. During the tests, photographs and video recordings were taken of some specimens to record the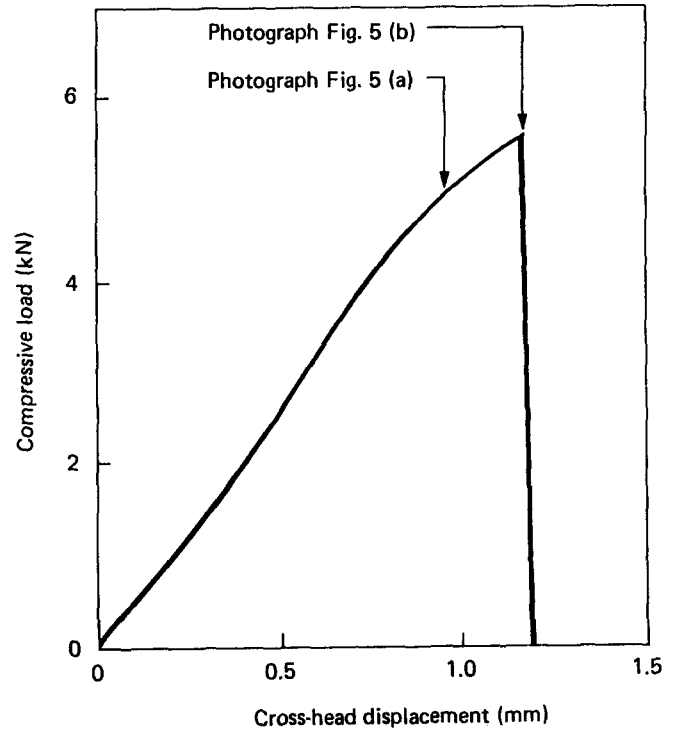 crack propagation process and some tests were stopped just before fracture to leave the specimens unbroken. Sections were cut from one of the unbroken specimens for micrographic examination. Burn-off tests[6] were conducted on samples cut from selected specimens to determine their glass content.

EXPERIMENTAL OBSERVATIONS AND RESULTS

The typical load vs cross-head displacement curve for tension–shear is shown in Fig. 2 and for compression–shear in Fig. 3. It can be seen that the curves are non-linear. In tension–shear the stiffness of the specimens decreased gradually with increasing load (see Fig. 2) until the specimen broke catastrophically. The non-linearity of these curves could be explained by the formation and propagation of cracks in the material. The crack length at various stages of loading can be measured from the photographs, see Fig. 4, or video recordings.

In both the tension–shear and compression–shear tests, a very large bending deformation was observed (see Fig. 5) and large transverse normal stresses occurred at the corners of the two notches. In tension, cracks were seen to initiate at the corners at very low load levels,
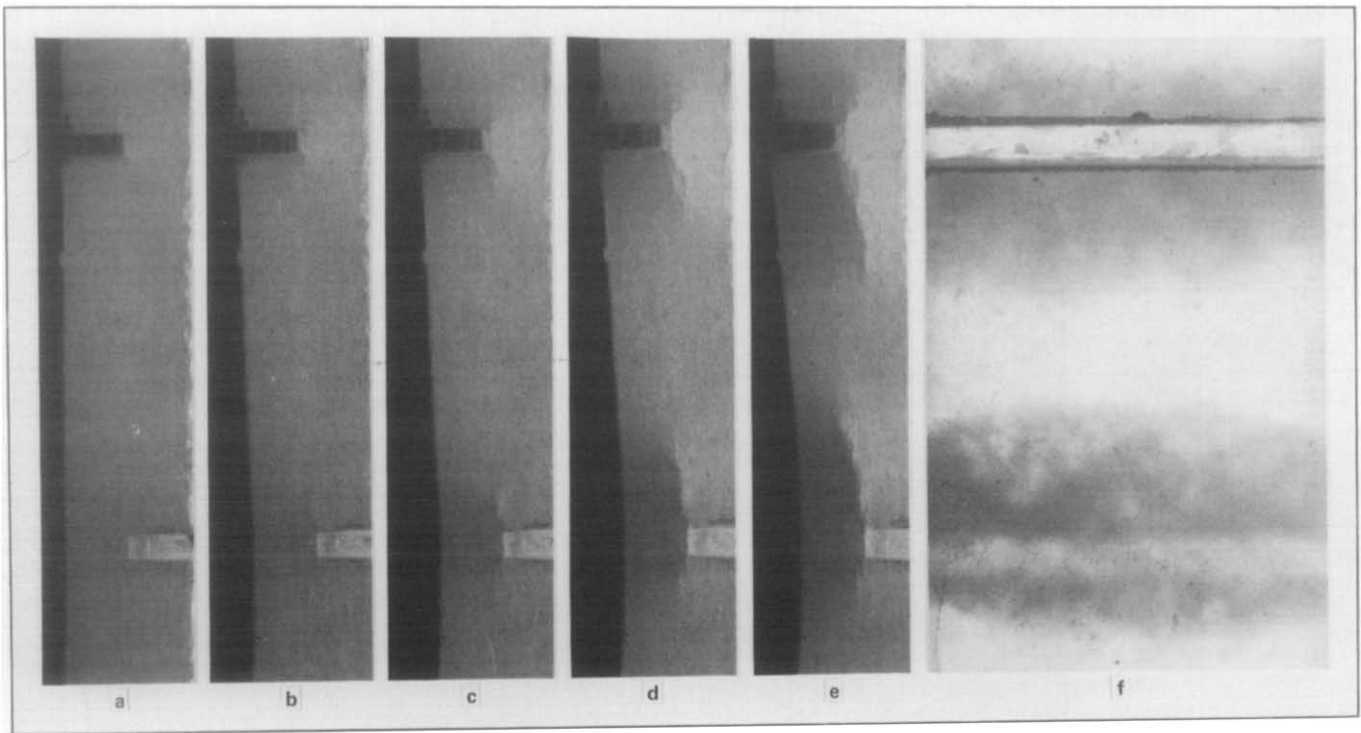
Fig. 4 (a)–(e) Crack developing in a shear specimen with increasing tensile load. The specimen is illuminated from the right. (f) as (e) but viewed from the left
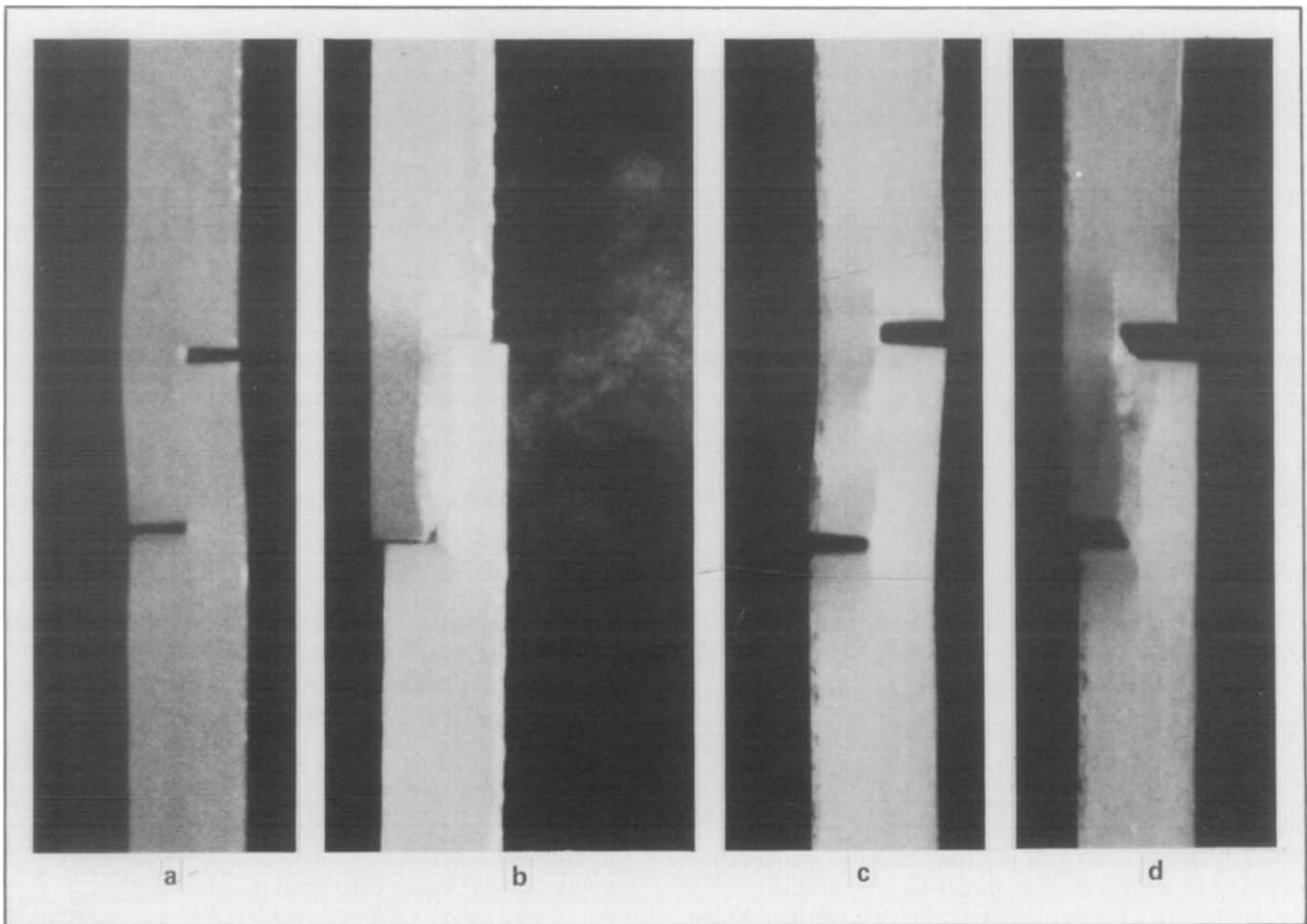

Fig. 5 (a) and (b) Shear specimen under compressive load (see Fig. 3); (c) and (d) another specimen under tensile load (see Fig. 2)

Table 2. Experimental results for tension tests on specimens cut from panel no 1

Specimen number	Thickness, t (mm)	Width, w (mm)	Length of shear surface, l (mm)	Maximum load, P (kN)	Shear strength, $\tau_{av} = P/(wl)$ (MPa)
2.1	8.4	24.95	12.0	4.67	15.6
2.2	8.3	25.0	12.1	4.81	15.9
2.3	8.25	24.9	12.5	4.63	14.8
2.4	8.4	24.9	12.1	4.45	14.75*
2.5	8.45	25.0	12.0	4.27	14.2
				Mean	15.13
				Standard deviation	0.77

Glass fraction 34.6% by weight
*Specimen unbroken — test stopped at 4.45 kN; result not included in calculation of mean

Table 3. Experimental results for tension tests on specimens cut from panel no 2

Specimen number	Thickness, t (mm)	Width, w (mm)	Length of shear surface, l (mm)	Maximum load, P (kN)	Shear strength, $\tau_{av} = P/(wl)$ (MPa)
3.1	11.68	24.95	12.5	4.21	13.49
3.2	12.15	25.08	12.8	3.56	11.08
3.3	11.79	24.92	13.5	4.21	12.5
3.4	12.2	24.95	15.0	3.64	9.71*
3.5	11.79	25.03	14.5	3.78	10.41
3.6	12.17	25.02	13.0	3.69	11.34
				Mean	11.76
				Standard deviation	1.2

Glass fraction 25.8% by weight
*Specimen unbroken — test stopped at 3.64 kN; result not included in calculation of mean

Table 4. Experimental results for tension tests on specimens cut from panel no 1

Specimen number	Thickness, t (mm)	Width, w (mm)	Length of shear surface, l (mm)	Maximum load, P (kN)	Shear strength, $\tau_{av} = P/(wl)$ (MPa)
4.1	8.69	25.8	25.0	4.14	6.42*
4.2	8.89	24.7	24.4	4.0	6.64
4.3	8.66	25.06	24.4	4.3	7.04
4.4	8.92	24.71	24.7	4.18	6.85
4.5	8.33	25.02	25.0	4.29	6.85
4.6	8.28	25.08	23.5	4.59	7.79
4.7	8.27	24.55	24.0	4.29	7.28
				Mean	7.07
				Standard deviation	0.41

Glass fraction 34.4% by weight
*Specimen unbroken — test stopped at 4.14 kN; result not included in calculation of mean

emitting faint noises and propagating in directions at a small angle to the load direction. When the cracks reached a certain (critical) length, they propagated rapidly parallel to the shear surface until reaching the other notch, then the specimen finally fractured.

The slope of the curve of compression load vs cross-head displacement (see Fig. 3) decreased only at high

loads and the maximum displacement of the cross-head was much less than that for the tension-shear case. The bending deformation tends to close the crack so during the stable cracking stage the crack was not as clear as in the tension-shear case. Another feature of the compression-shear tests was that, as the load increased and the crack extended, puffs of smoke-like dust (see Fig. 5(b)) were emitted, together with faint noises.

Table 5. Experimental results for tension tests on specimens cut from panel no 3

Specimen number	Thickness, t (mm)	Width, w (mm)	Length of shear surface, l (mm)	Maximum load, P (kN)	Shear strength, $\tau_{av} = P/(wl)$ (MPa)
5.1	9.1	24.88	12.0	3.73	12.45
5.2	8.87	24.95	12.5	3.78	12.06
5.3	8.98	24.75	13.2	3.66	11.17
5.4	8.88	25.06	13.0	3.87	11.86
5.5	8.31	25.03	12.5	4.56	14.6
				Mean	12.43
				Standard deviation	1.2

Glass fraction 32.3% by weight

Table 6. Experimental results for compression tests on specimens cut from panel no 3

Specimen number	Thickness, t (mm)	Width, w (mm)	Length of shear surface, l (mm)	Maximum load, P (kN)	Shear strength, $\tau_{av} = P/(wl)$ (MPa)
6.1	8.27	25.02	11.5	5.59	19.4
6.2	8.16	24.75	13.0	5.2	16.17*
6.3	8.59	25.01	12.0	5.4	17.43
6.4	8.81	24.94	12.2	5.35	17.54
6.5	8.98	25.04	11.7	5.44	18.52
				Mean	18.22
				Standard deviation	0.93

Glass fraction 31.4% by weight
*Specimen unbroken — test stopped at 5.2 kN; result not included in calculation of mean

The test results for the 28 specimens are listed in Tables 2–6. The consistency of the tests was good and the standard deviation of the data for each group of specimens was small. The shear strength was defined[1] as the maximum load divided by the nominal area in shear ($\tau_{av} = P/wl$). For tension–shear tests the failure loads were all roughly the same so that specimens having the longer shear surface gave lower shear strengths than the shorter specimens. Note that the 12 mm long specimens (Table 2) were cut from the same panel (panel 1) as the 25 mm long specimens of Table 4. Comparing the results from Tables 2, 3 and 5 shows that panels with lower mass fractions of fibres tended to have lower shear strengths. Comparing the results of tension–shear and compression–shear tests for specimens having the same length of shear surface and cut from the same panel (panel no 3), compression loading resulted in larger shear strength than tension loading (see Tables 5 and 6).

In Fig. 4, six photographs show the crack propagation process for a tension–shear specimen with the longer shear surface. The crack initiated from the inner corner of a notch and extended initially in a direction roughly parallel to the loading direction, turned through a small angle and then propagated along the specimen again. As a result of this process a 'stair-like' crack pattern was formed. The gross angle of the crack to the load direction was approximately 10–15°. After the specimen broke, a very rough crack resulted with a large number of fibres crossing it.

Four samples were cut from a cracked but unbroken specimen and studied by photomicrography. A series of photographs were taken. From the photographs (see Figs 6 and 7) it is clear that the cracks tend to pass along the specimen through fibre-congested zones and cut at an angle across resin-rich zones. It has been shown previously[7,8] that fractures in E-glass fibre/polyester composites tend to occur at or near to fibre/resin interfaces. Since the fibre bundles in the chopped strand mat tend to be flattened in the plane of the laminate (see Fig. 6), the cracks propagate through these bundles in a direction roughly parallel to the surface of the laminate whereas in the resin, which is isotropic, the cracks tend to propagate in directions
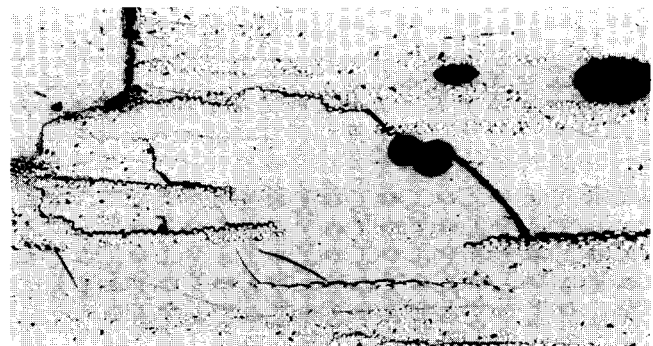

Fig. 6 Micrograph showing cracks developing from the corners of a notch (the notch is at top left)
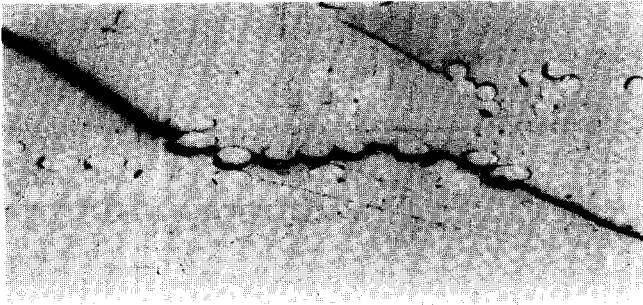
Fig. 7 Micrograph showing typical crack propagation across resin-rich areas and through a bundle of fibres
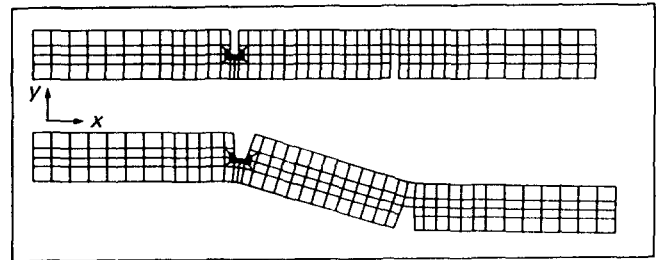

Fig. 8 Undeformed and deformed mesh pattern 1

Fig. 9 Undeformed and deformed mesh pattern 2 with transverse constraint of centre node at right-hand end

perpendicular to the directions of maximum tensile stress. This is the mechanism of the formation of stair-like crack paths. The photographs reveal clearly the inhomogeneity of the distribution of the glass fibres in the matrix resin which, together with some other imperfections such as voids, have a great influence on the path of the crack.

FINITE ELEMENT ANALYSIS

Finite element formulation

Two-dimensional eight-node quadrilateral iso-parametric elements were adopted. The formulation of this element was given in Reference 9. Collapsed triangular quarter-point singular elements[10] were used in the calculation of mixed-mode stress intensity factors K_I and K_{II}, while the normal elements were used in the analysis of stress distributions.

Material model

Two different material models were assumed: isotropic and orthotropic. In both cases the material was treated as homogeneous. For the isotropic model,[11] $E = 7.0$ GPa and $v = 0.34$; whereas for the orthotropic model, $E_x = 9.81$ GPa, $E_y = 5.20$ GPa, $v_{xy} = 0.34$ and $G_{xy} = 1.43$ GPa (for 37% by weight E-glass CSM in polyester).[11,12]

Boundary conditions

One end of the specimen was assumed to be fixed with no translation or rotation allowed. The other end was subject to uniform traction. No rotation constraint was imposed on this end but in some cases the central node point was constrained not to translate in the transverse direction (see Figs 8 and 9).

Stress distribution

Stress distributions were calculated using two mesh patterns (see Figs 8 and 9). As expected, there was little difference between the results except that slightly higher stresses were obtained at the notch for mesh pattern 1 (Fig. 8) which has smaller elements at the corner of the notch. If the elements were made infinitesimally small, the stresses at a sharp corner are expected to approach infinity. Changing the constraints from those shown in Fig. 8 to those in Fig. 9 did not alter the results significantly.

Fig. 10 shows the shear stress (τ) distribution along the shear surface calculated using the mesh pattern and
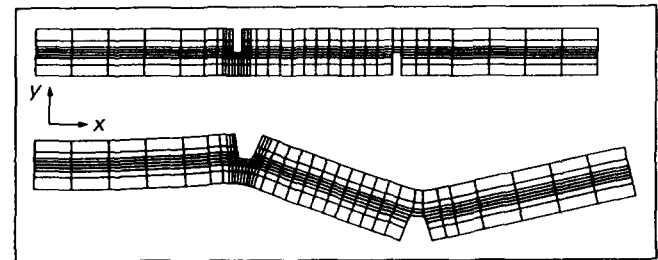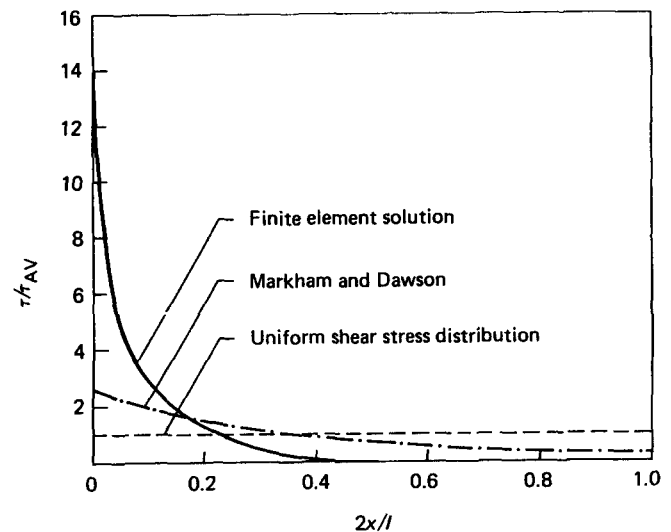

Fig. 10 Variation of shear stress with distance along the gauge length measured from the corner of the notch
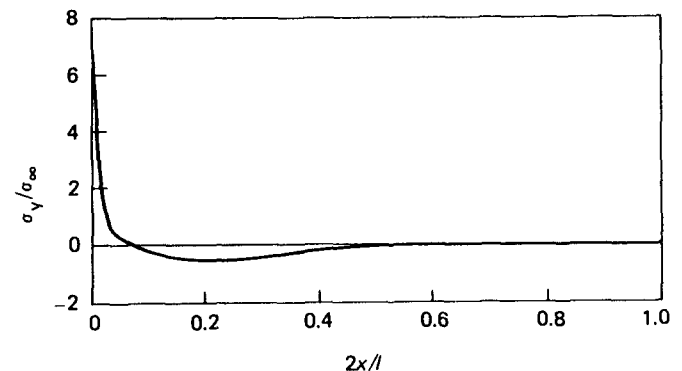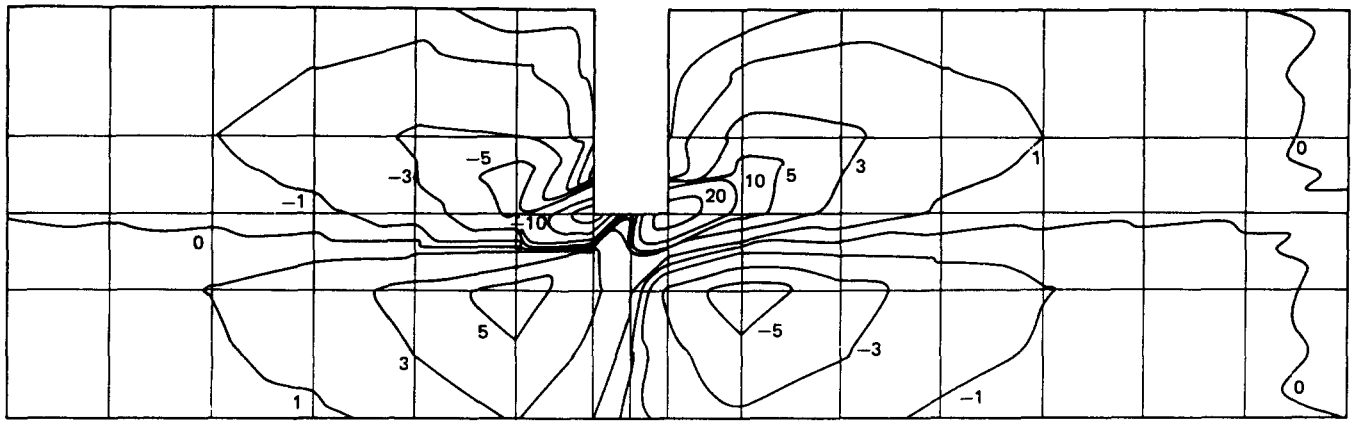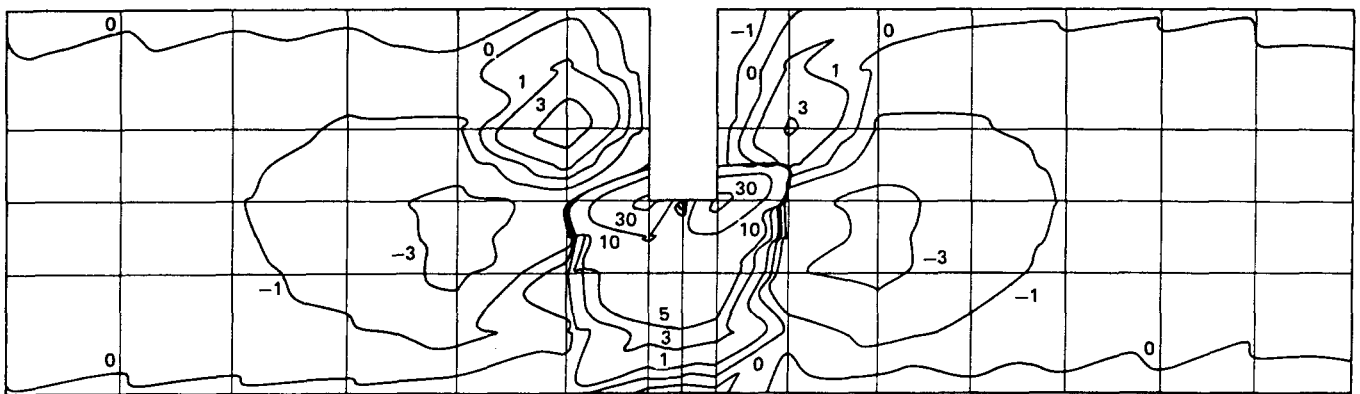

Fig. 11 Variation of transverse normal stress with distance along the gauge length

constraints of Fig. 8 and isotropic material properties. Also shown in Fig. 10 are the shear stress curves calculated using the formula given by Markham and Dawson[3] and the nominal uniform shear stress

a

b

Fig. 12 (a) Shear; and (b) transverse normal stress distributions. Contours are lines of constant stress and numbers on the contours indicate the stress magnitude (MPa) when $\sigma_\infty = 8$ MPa. Half of the gauge length and the second notch (to the right of each figure) has been omitted

distribution as used in the calculations for shear strength. The transverse normal stress (σ_y) distribution along the shear surface is shown in Fig. 11. Both shear stress and transverse stress graphs show a very large stress concentration at the notch. It is these stress concentrations which are the main cause of the damage, cracking and failure of the specimen. Stresses calculated using the orthotropic material properties were very similar to those for the isotropic case, except that the peak shear stresses and transverse tensile stresses at the corner of the notch were 25% lower for the orthotropic material. Shear stress (τ) contours and transverse normal stress (σ_y) contours were calculated using finite element mesh pattern 1 (Fig. 8) with orthotropic material properties. The results are shown in Fig. 12.

Figs 13(a)-(c) show the theoretical shear stress distributions for three models having different shear lengths between notches; in all other respects the model specimens are the same. Mesh pattern 1 was employed with orthotropic properties. The 25 mm shear length (Fig. 13(a)) corresponds to the longer length used in the experiments and to the theoretical results discussed previously. The 12.5 mm length (Fig. 13(b)) corresponds to the shorter length used in the experiments and is also the standard length recommended in BS4994. Comparison of Figs 13(a) and (b) shows that the stress distribution near the

notch is the same in both cases, which explains why the shear strengths obtained from the experiments were larger for the shorter specimens. The method for calculating shear strength implied a uniform stress distribution. The shear distribution for the 12.5 mm length is still far from uniform, the shear stress being nearly zero over a significant fraction of the shear length. The results for the shortest (6.25 mm) length model (Fig. 13(c)) show that the shear length would have to be much shorter than the standard length for a more uniform stress distribution to be achieved. The shear stress distribution also varies with specimen thickness, thicker specimens having more uniform stress distribution.

Prediction of crack initiation

Calculations for predicting the crack initiation and the likely extent of the microcracked zone were carried out for a model with a 25 mm shear length and orthotropic elastic properties using the mesh shown in Fig. 9. Within every element the strains and stresses at 25 (5 x 5) points (including nine Gauss sampling points and eight nodal points) can be calculated. In each load step a search was conducted to find the maximum stress and its position. If the stress is larger than a critical value, microcracks will appear and fracture will occur at that position. The following criteria were employed in the computation.[13]
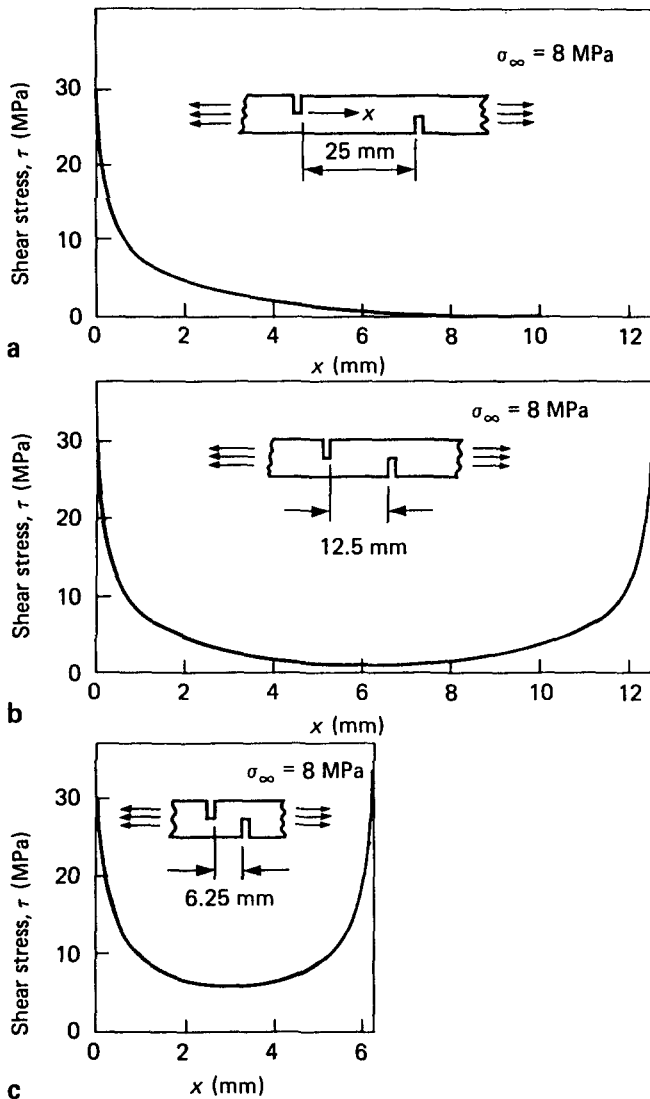
Fig. 13 Effect of shear length on shear stress distribution for shear lengths of: (a) 25 mm; (b) 12.5 mm; and (c) 6.25 mm

1. Maximum stress failure criteria

$$\sigma_x \leqslant \sigma_{xc}$$

$$\sigma_y \leqslant \sigma_{yc} \tag{1}$$

$$\tau \leqslant \tau_c$$

2. Norris distortional energy failure criteria

$$\phi = [(\sigma_x/\sigma_{xc})^2 + (\sigma_y/\sigma_{yc})^2 - (\sigma_y\sigma_x/\sigma_{yc}\sigma_{xc})^2$$

$$+ (\tau/\tau_c)^2]^{1/2} \leqslant 1 \tag{2}$$

In the above two criteria, σ_x, σ_y and τ are the parallel, transverse and shear stresses, respectively, and σ_{xc}, σ_{yc} and τ_c are their critical values. From the limited experimental data available[11,12] it was assumed that:

$$\sigma_{xc} = 120\,\text{MPa}, \quad \sigma_{yc} = 9\,\text{MPa} \quad \text{and} \quad \tau_c = 29\,\text{MPa} \tag{3}$$

It must be noted that the through-thickness data is subject to doubt.

Table 7. Prediction of initial failure strengths

	Criteria			
	$\sigma_x \leqslant \sigma_{xc}$	$\sigma_y \leqslant \sigma_{yc}$	$\tau \leqslant \tau_c$	$\phi \leqslant 1$
Initial failure strength, σ_∞ (MPa)	20.2	2.45	11.11	2.1

The initial failure point predicted by all the different criteria was the inner corner point of the notch. Table 7 shows the initial failure strengths predicted by the different criteria. It can be concluded from Table 7 that, as expected, the distortional strain energy criterion, $\phi \leqslant 1$, predicts earlier damage than other criteria (damage starting when $\sigma_\infty \doteq 2.1$ MPa in this model), and the maximum stress criterion predicts failure due to transverse tension at a slightly higher strength. Although this is nominally a shear test, the maximum stress criterion predicts failure by transverse tension rather than shear.

When the stress (or stress factor ϕ) value meets the failure criteria (1) or (2), the material at this point fails and the corresponding material modulus must be changed. For simplicity it was assumed that if $\tau \geqslant \tau_c$, then $G_{xy} = 0$; if $\sigma_y \geqslant \sigma_{yc}$, then $E_y = \nu_{yx} = 0$; if $\sigma_x \geqslant \sigma_{xc}$, then $E_x = \nu_{xy} = 0$; and if $\phi \geqslant 1$, then $E_x = E_y = \nu_{xy} = \nu_{yx} = G_{xy} = 0$. Other points in the element remained unchanged. The stiffness matrix was reformed and the whole calculation cycle repeated and a search conducted for the next maximum stress point; hence the crack propagation direction was found. Using the procedure described above, the initial crack propagation direction predicted by all the criteria (1) and (2) is along the load direction (x), which coincides with the observation in the micrographs, see Fig. 6. Repeating the above calculations predicts narrow damage zones near the corners of the notches. The term damage zone is used rather than crack because the analysis assumed that, at points where failure has occurred, the material has not separated but is still contiguous. This is an analytical rather than a physical model. A physical representation would be a damaged or microcracked region which exists before formation of the macrocrack. The damaged zone predicted by the
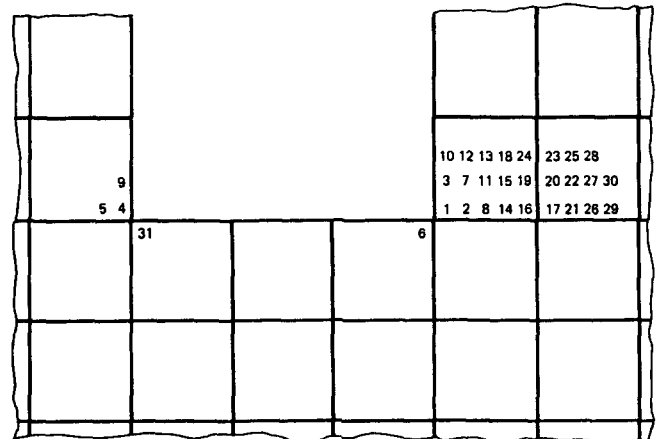
Fig. 14 Damage zone near the corner of a notch predicted using the maximum normal stress criterion of failure ($\sigma_y \leqslant \sigma_{yc}$). The numbers show position and sequence in which predicted failures occurred
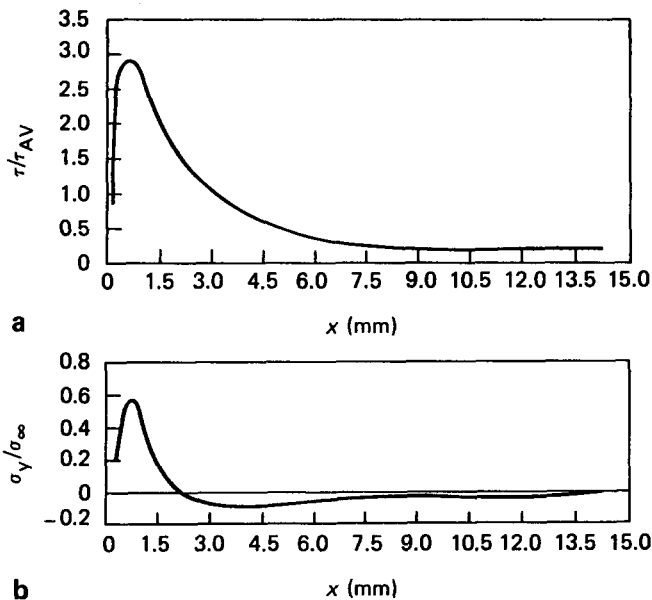
Fig. 15 (a) Shear: and (b) transverse normal stress distributions predicted at a line of elements next to the shear surface in a specimen with a small damage zone at the corner of the notch

maximum transverse normal stress failure criterion, $\sigma_y \leqslant \sigma_{yc}$ is shown in Fig. 14. The applied load was equivalent to a fairly low tensile load of approximately 5 MPa (see Fig. 2) and the damage zone was about 1.2 mm long. The numbers in Fig. 14 show the sequence in which failure occurred. The stress distribution of average stresses for the line of elements adjacent to the shear surface is shown in Fig. 15 for the same applied load of 5 MPa but using the failure criterion $\phi \leqslant 1$. Comparing Figs 15(a) and (b) with

Figs 10 and 11 it can be seen that the stress distributions are changed significantly by the presence of the damaged zone and, in the damaged area, the stress values decrease greatly.

Mixed-mode stress intensity factors

The mixed-mode stress intensity factors K_I and K_{II} were calculated using mesh pattern 3 shown in Fig. 16. A crack was embedded in the shear surface and 24 special elements were patched in the vicinity of the crack. Around the crack tip there were eight collapsed, triangular, quarter-point singular elements. The three collapsed nodes in each element were constrained to have the same displacement. These elements possess $1/\sqrt{r}$ singularity of strain.

The crack propagation process was calculated using a constraint release technique, and the diagrams of the deformed grids at three stages of crack propagation are shown in Fig. 16(b), (c) and (d).

The relationship between K_I and K_{II} and the finite element displacement field is given as:[14]

$$
U_r = K_I\sqrt{(2r/\pi)} \ Re\left[\frac{1}{m_1-m_2}(m_1 p_2\sqrt{\cos\theta + m_2\sin\theta}\right.
$$
$$
\left. - m_2 p_1\sqrt{\cos\theta + m_1\sin\theta}\right]
$$
$$
+ K_{II}\sqrt{(2r/\pi)} \ Re\left[\frac{1}{m_1-m_2}(p_2\sqrt{\cos\theta + m_2\sin\theta}\right.
$$
$$
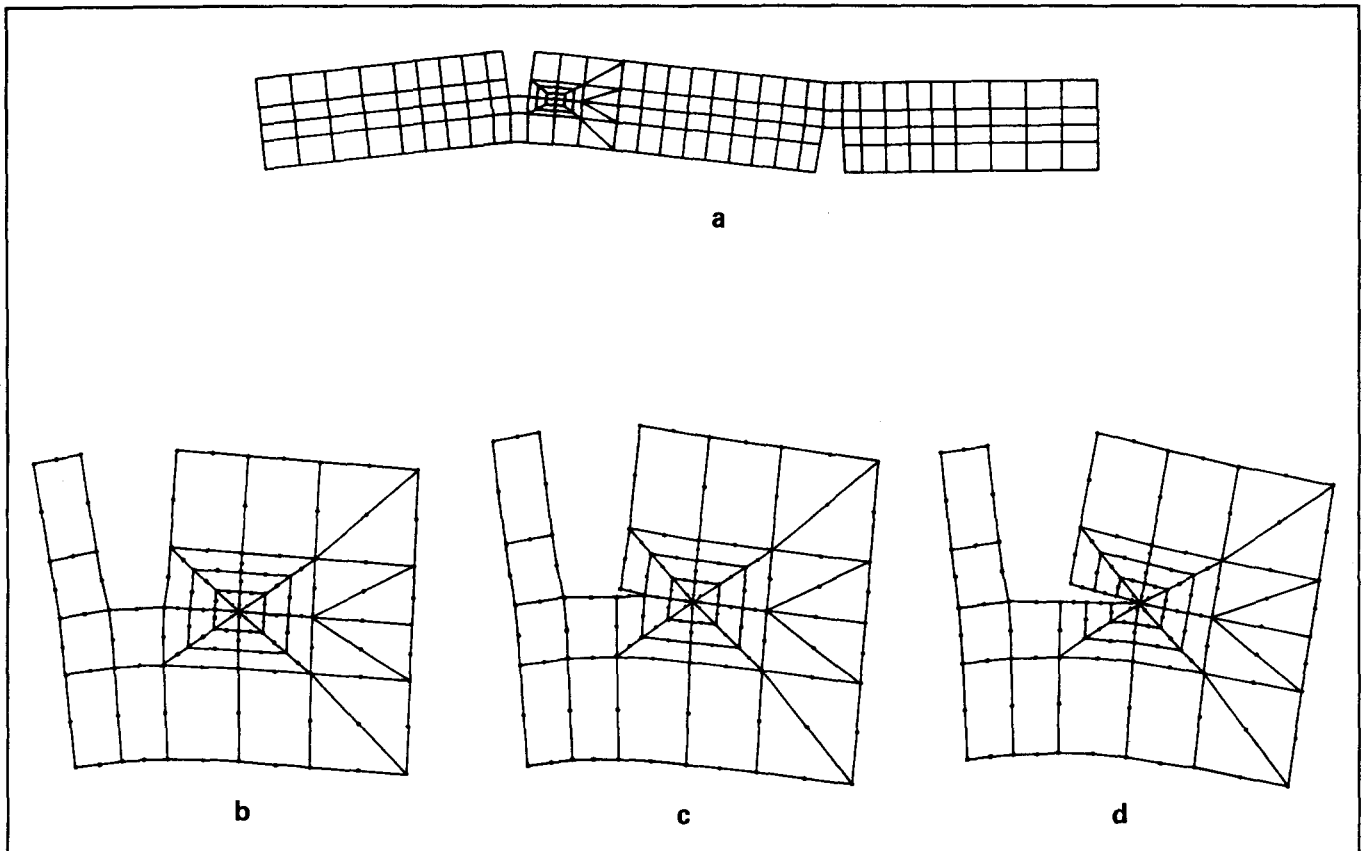\left. - p_1\sqrt{\cos\theta + m_1\sin\theta}\right] \tag{4}
$$

Fig. 16 Mesh used to represent a specimen with a crack. (b), (c) and (d) show details of the grid representing progressive crack propagation

$$U_\theta = K_I\sqrt{(2r/\pi)}\,Re\left[\frac{1}{m_1-m_2}\,(m_1 q_2\sqrt{\cos\theta + m_2\sin\theta}\right.$$

$$\left. - m_2 q_1\sqrt{\cos\theta + m_1\sin\theta}\right]$$

$$+ K_{II}\sqrt{(2r/\pi)}\,Re\left[\frac{1}{m_1-m_2}\,(q_2\sqrt{\cos\theta + m_2\sin\theta}\right.$$

$$\left. - q_1\sqrt{\cos\theta + m_1\sin\theta}\right] \tag{5}$$

where m_1 and m_2 are two different roots of the following equation, and they always occur in conjugate pairs as m_1, $\overline{m}_1$ and m_2, $\overline{m}_2$:

$$a_{11}m^4 - 2a_{16}m^3(2a_{12} + a_{66})m^2 - 2a_{26}m + a_{22} = 0 \tag{6}$$

p_i and q_i are defined as:

$$p_i = a_{11}\cdot m_i^2 + a_{12} - a_{16}m_i \tag{7}$$

$$q_i = a_{12}m_i + a_{22}/m_i - a_{26} \tag{8}$$

where a_{ij} are compliance coefficients:

$$\epsilon_i = \sum a_{ij}\sigma_j \tag{9}$$

Using the displacement distribution on the two crack surfaces ($\theta = \pm\pi$) is the simplest way to obtain K_I and K_{II} and gives more accurate results.

$$K_I(\pi) = \sqrt{(\pi/2r_0)}\left[\frac{U_\theta(r_0\pi)}{F_I}\right] \quad (\theta = \pi) \tag{10}$$

$$K_I(-\pi) = \sqrt{(\pi/2r_0)}\left[\frac{U_\theta(r_0 -\pi)}{F_I}\right] \quad (\theta = -\pi) \tag{11}$$

$$K_I = [K_I(\pi) - K_I(-\pi)]/2 \tag{12}$$

$$K_{II}(\pi) = \sqrt{(\pi/2r_0}\left[\frac{U_r(r_0\pi)}{F_{II}}\right] \quad (\theta = \pi) \tag{13}$$

$$K_{II}(-\pi) = \sqrt{(\pi/2r_0}\left[\frac{U_r(r_0 -\pi)}{F_{II}}\right] \quad (\theta = -\pi) \tag{14}$$

$$K_{II} = [K_{II}(\pi) - K_{II}(-\pi)]/2 \tag{15}$$

where F_I and F_{II} can be calculated by using Equations (4)–(9).

The polar coordinate system in the vicinity of the crack tip is shown in Fig. 17.

It can be seen in Equations (10)–(15) that K_I and K_{II} depend on r_0, the distance from the crack tip to an arbitrary point on the crack surface. In the present paper, the following formulae, given in Reference 15, were used to obtain the stress intensity factors at the crack tip:

Table 8. Prediction of stress intensity factors

Stress intensity factor	Critical stress intensity factors
$K_I/\sigma_\infty\sqrt{a} = 1.383$	$K_{Ic} = 2.29$ MPa $M^{1/2}$
$K_{II}/\sigma_\infty\sqrt{a} = 2.285$	$K_{IIc} = 3.78$ MPa $m^{1/2}$

$$K_I = [\sqrt{\pi}/(F_I\sqrt{2})]\,[(4U_{\theta B}-U_{\theta C})/\sqrt{L}] \tag{16}$$

$$K_{II} = [\sqrt{\pi}/(F_{II}\sqrt{2})]\,[(4U_{rB}-U_{rC})/\sqrt{L}] \tag{17}$$

where $U_{\theta B}$, $U_{\theta C}$, U_{rB} and U_{rC} are circumferential and radial displacements at B and C respectively, see Fig. 18.

The values of K_I and K_{II} corresponding to the deformation shown in Fig. 16(d) are listed in Table 8, together with the critical stress intensity factors K_{Ic} and K_{IIc}, estimated for a failure load of 20 MPa and a critical crack length of 6.5 mm which are typical of the load and crack lengths observed just before failure in the experiments.

CONCLUSIONS

The single lap shear test method specified in BS4994 was examined to evaluate its suitability for measuring the interlaminar shear strength of CSM-GRP laminates. Experiments have shown that the apparent shear strength determined by this method is influenced greatly by the length between the notches, with a longer length giving lower shear strength.

During the tests, cracks started at the corners of the notches and extended to about 50% of the specimen
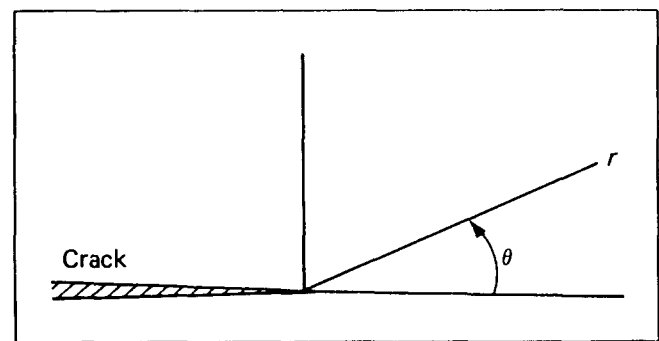

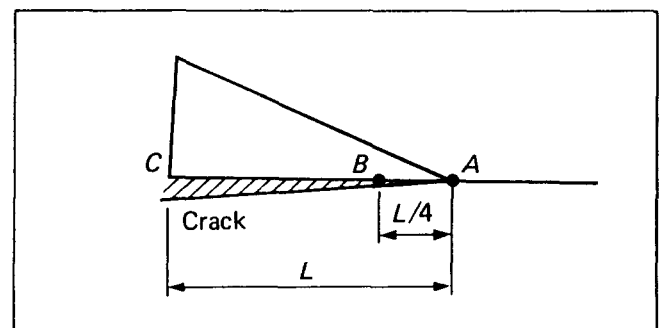Fig. 17   Polar coordinates at the crack tip

Fig. 18   Quarter-point element

shear length before failure finally occurred. The micrographic investigation showed that the cracks tended to follow the fibre/matrix interface and the distribution of fibres appeared to influence the orientation of the cracks.

Large bending deformation was observed in both tension–shear and compression–shear tests and significant through-thickness normal stresses occurred. In compression–shear, these through-thickness stresses are compressive and tend to close the cracks, resulting in higher shear strengths.

The stress distribution along the shear surface obtained by finite element analysis showed large stress concentrations at the corners of the notches, which were the cause of cracking of the material and of the variation of shear strength with shear surface length.

The highly non-uniform stress distribution and the possibility of failure initiation by transverse forces makes this a poor method of measuring shear strength and the results cannot reasonably be used directly as a shear stress in engineering design calculations.

The finite element analysis of the damage zone and mixed-mode stress intensity factors gives some insight into the fracture mechanism and redistribution of stresses in the cracked specimen. Use of the maximum stress failure criterion predicted inital failure due to transverse tension rather than shear. The estimation of the critical stress intensity factors K_{Ic} and K_{IIc} may provide material properties to characterize the resistance to cracking of this material under this type of loading.

REFERENCES

1 BS4994, Specification for Vessels and Tanks in Reinforced Plastics (BSI, London, 1973)
2 Chiao, C.C., Moore, R.I. and Chiao, T.T. 'Measurement of shear properties of fibre composites, Part 1. Evaluation of the test methods' Composites 9 No 3 (July 1977) pp 161–169
3 Markham, M.F. and Dawson, D. 'Interlaminar shear strength of fibre reinforced composites' Composites 6 No 3 (July 1975) pp 173–176
4 Zhang Shuangyin 'A study on interlaminar shear strength of composites' Proc 4th Int Conf on Mechanical Behaviour of Materials, Stockholm, Sweden, August 1983 1 pp 565–571
5 BS3496, E Glass Fibre Chopped Strand Mat for the Reinforcement of Polyester Resin Systems (BSI, London, 1973)
6 BS2782, British Standard Methods of Testing Plastics, Part 10: Glass Reinforced Plastics (BSI, London, 1977)
7 Owen, M.J. 'Fatigue testing of fibre reinforced plastics' Composites 1 No 6 (December 1970) pp 346–355
8 Hull, D. 'An Introduction to Composite Materials' (Cambridge University Press, UK, 1981)
9 Owen, D.R.J. and Hinton, E. 'Finite Elements in Plasticity, Theory and Practice' (Pineridge Press Limited, Swansea, UK, 1980)
10 Barsoum, R.S. 'Triangular quarter-point elements as elastic and perfectly-plastic crack tip elements' IJNME 11 (1977) pp 85–98
11 Barton, D.C. and Soden, P.D. 'Short term in-plane stiffness and strength properties of CSM reinforced polyester laminates' Composites 13 No 1 (January 1982) pp 66–78
12 Kitching, R., Tan, A.L. and Abu Mansour, T.M.N. 'The influence of through thickness properties on glass reinforced plastic laminated structures' Composite Structures 1 No 2 (1984) pp 105–151
13 Owen, M.J. 'Biaxial failure of GRP — mechanisms, modes and theories' Proc 2nd Int Conf on Composite Structures, Paisley College of Technology, Scotland, 14–16 September 1983 (Applied Science Publishers, UK, 1983) pp 21–39
14 Wang, S.S., Yau, J.F. and Corten, H.T. 'A mixed-mode crack analysis of rectilinear anisotropic solids using conservation laws of elasticity' Int J Fracture 16 No 3 (June 1980) pp 247–259
15 Shih, C.F., DeLorenzi, H.G. and German, M.D. 'Crack extension modelling with singular quadratic isoparametric elements' Int J Fracture 12 (1976) pp 647–651

AUTHORS

S.Y. Zhang is with the Institute of Mechanics, Chinese Academy of Sciences, Beijing, People's Republic of China. P.D. Soden, to whom inquiries should be addressed, and P.M. Soden are with the Department of Mechanical Engineering, UMIST, PO Box 80, Manchester, M60 1QD, UK.